Sequential Cation Exchange Generated Superlattice Nanowires Forming Multiple p–n Heterojunctions

Chih-Shan Tan,[†] Ching-Hung Hsiao,[†] Shau-Chieh Wang,[†] Pei-Hsuan Liu,[†] Ming-Yen Lu,[‡] Michael H. Huang,[§,*] Hao Ouyang,[†] and Lih-Juann Chen[†,*]

[†]Department of Materials Science and Engineering, National Tsing Hua University, Hsinchu 30013, Taiwan, [‡]Graduate Institute of Opto-Mechatronics, National Chung Cheng University, Chiayi 62102, Taiwan, and [§]Department of Chemistry, National Tsing Hua University, Hsinchu 30013, Taiwan

ABSTRACT Fabrication of superlattice nanowires (NWs) with precisely controlled segments normally requires sequential introduction of reagents to the growing wires at elevated temperatures and low pressure. Here we demonstrate the fabrication of superlattice NWs possessing multiple p–n heterojunctions by converting the initially formed CdS to Cu_2S NWs first and then to segmented Cu_2S–Ag_2S NWs through sequential cation exchange at low temperatures. In the formation of Cu_2S NWs, twin boundaries generated along the NWs act as the preferred sites to initiate the nucleation and growth of Ag_2S segments. Varying the immersion time of Cu_2S NWs in a $AgNO_3$ solution controls the Ag_2S segment length. Adjacent Cu_2S and Ag_2S segments in a NW were found to display the typical electrical behavior of a p–n junction.

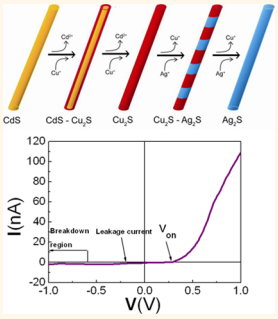

KEYWORDS: superlattice · heterojunction · p–n diode · cation exchange

In the past decade, synthesis of new heterojunction[1–5] and superlattice[6–10] NWs has been an exciting and challenging development owing to their versatile properties in nanoelectronic and nanophotonic functions.[11–16] Previously, the main concept for the formation of heterojunction superlattice NWs is alternating the reactant precursors consecutively with varying time.[17–19] A critical step is to use different structural transformations locally in a NW to create a desirable heterojunction superlattice NW. By precise control of the process, different kinds of heterojunctions and lengths of heterosegments can be formed which can substantially increase the applicability of NWs. Robinson *et al.* synthesized CdS–Ag_2S superlattice (n–n junction) nanorods under low temperature and pointed out that this self-organization is driven by lattice-mismatch strain.[20] Here we report a sequential cation exchange process which transforms single-crystal NWs to twinning NWs and eventually to superlattice p–n heterojunction NWs. Specifically, CdS NWs were used as a template to form CdS–Cu_2S core–shell NWs and subsequently twinning Cu_2S NWs through cation exchange. The twinning Cu_2S NWs were then transformed to Cu_2S–Ag_2S p–n heterojunction superlattice NWs with tunable segment lengths *via* further cation exchange of Cu^+ by Ag^+ with precise control of reaction time. Features of selective facet reactivity[21,22] and sequential cation exchange ability[23,24] are exhibited. Heterojunctions in NWs are facilitated due to higher endurance of lattice mismatch and a lower density of dislocations than those in thin films.[25] The neighboring segments of Cu_2S–Ag_2S superlattice NWs display typical electrical behavior of p–n junctions. The process represents a novel route to tailor-made heterojunction NWs.

A new approach for synthesizing superlattice NWs is to spontaneously introduce local structural defects, such as twins, along the length of a single-component NW. Twin is a common defect in atomic replacement reactions,[26] and we utilized twin boundaries as preferred sites for the cation exchange process to form heterojunctions. Precise control of the ionic diffusion process enables the formation of heterosegments with tunable lengths. Proper selection of the materials to constitute the alternate segments can realize the generation of p–n junctions in

* Address correspondence to ljchen@mx.nthu.edu.tw, hyhuang@mx.nthu.edu.tw.

Received for review June 29, 2014 and accepted August 19, 2014.

Published online August 25, 2014
10.1021/nn5035247

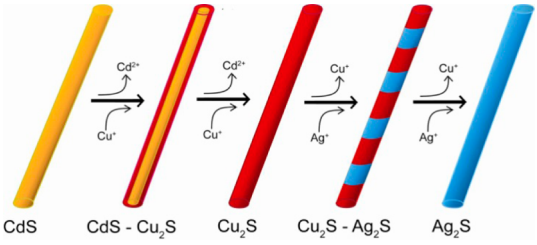

Figure 1. Chain cation exchange process to form superlattice NWs with multiple p–n heterojunctions. Illustration of the complete experimental process for the formation of Cu_2S–Ag_2S superlattice NWs.

the NWs. Figure 1 illustrates the synthetic sequence to form Cu_2S–Ag_2S superlattice NWs from CdS NWs. Twins are introduced in the Cu_2S NWs after exchanging Cd^+ with Cu^+. The locations of these twin boundaries are sites for preferential Cu^+ replacement with Ag^+ and dictate the initial separation of the Ag_2S segments.

RESULTS AND DISCUSSION

Single-crystalline CdS NWs, of $P6_3/mmc$ space group, were grown by the vapor–liquid–solid (VLS)[27] process (see Supporting Information Figure S1). The CdS NWs were converted to CdS–Cu_2S core–shell NWs in the first cation exchange process. After 1 min reaction, Cu^+ efficiently replaces Cd^{2+} to form Cu_2S shells over the CdS NWs (see Supporting Information Figure S2). Scanning transmission electron microscopy energy-dispersive spectroscopy (STEM-EDS) mapping images clearly reveal this core–shell structure. When this cation exchange process is maintained for 25 min, the core–shell NWs transform completely into pure Cu_2S NWs. X-ray diffraction (XRD) patterns of the NWs confirm the conversion from CdS to Cu_2S (see Supporting Information Figure S3), of $F\bar{4}3m$ space group, with a face-centered cubic (fcc) crystal structure. From the partial Cu–S phase diagram, fcc Cu_2S is a stable phase at temperatures greater than 435 °C. It indicates that cation exchange is a method to fabricate a high-temperature phase in a lower temperature environment (see Supporting Information Figure S4 and Figure S5) .

Transmission electron microscopy (TEM) images of a single Cu_2S NW reveals the presence of extensive twinning with twin planes perpendicular to the growth direction of the NW (Figure 2a). A selected-area electron diffraction (SAED) pattern obtained from the NW taken along the [110] zone axis with fast Fourier transform (FFT) process indicates that the twin planes are the $(1\bar{1}1)$ planes with streaking along the $[1\bar{1}1]$ direction (Figure 2b). Figure 2c is a FFT-processed TEM image of the red framed region in Figure 2a. The $(\bar{1}11)$ lattice planes (yellow line) make zigzag changes to mirror planes along the length of the NW at the $(1\bar{1}1)$ twin boundaries (green lines). The formation of these twins is induced by large strain energy accompanied by not only the conversion of hexagonal close-packed

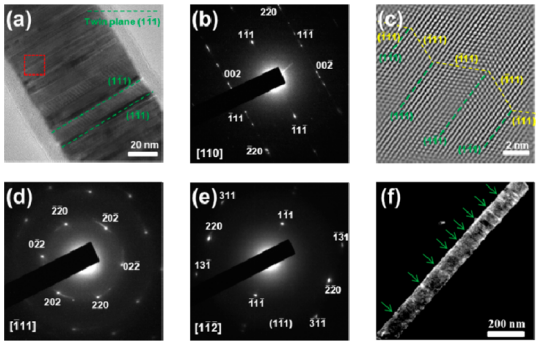

Figure 2. TEM characterization of single Cu_2S NWs. (a) TEM image of a Cu_2S NW transformed from a CdS NW. The twin planes are the $(1\bar{1}1)$ planes. (b) FFT pattern of a Cu_2S NW recorded along the [110] zone axis, revealing streakings owing to the presence of a high density of twins with the $(1\bar{1}1)$ twin plane. (c) FFT-processed HRTEM image of the framed region in panel a. Twin structures are clearly visible in this image. (d) SAED pattern of a Cu_2S NW recorded along the $[\bar{1}11]$ zone axis. The appearance of streaks in addition to the diffraction spots shows multidomain structure of the NW. (e) SAED pattern of a Cu_2S NW recorded along the $[1\bar{1}2]$ zone axis. Streaks are also present. (f) Dark-field TEM image of a single Cu_2S NW viewed along the [110] zone axis and presented by selecting the $(1\bar{1}1)$ diffracted beam. The green arrows indicate locations of the $(1\bar{1}1)$ twins.

CdS into fcc Cu_2S but also the large cation diameter difference (109 pm for Cd^{2+} *vs* 91 pm for Cu^+). When SAED patterns of the NW were taken along the $[\bar{1}11]$ and $[1\bar{1}2]$ zone axes, streaks could be clearly seen in addition to the regular single-crystalline diffraction spots (Figure 2d,e), suggesting that the NW possesses lattice domains with slightly misaligned lattice planes, as seen in the high-resolution (HR) TEM images. Figure 2f is the dark-field image of the twinned Cu_2S NW imaged with a $(1\bar{1}1)$ diffraction beam. The $(1\bar{1}1)$ twins are evident with bright contrast and are pointed out by green arrows.

The Cu_2S NWs were converted to Cu_2S–Ag_2S superlattice heterojunction NWs in the second cation exchange process. Ag_2S is an n-type semiconductor with a monoclinic crystal structure belonging to the $P2_1/c$ space group. Figure 3 illustrates the formation and gradual elongation of Ag_2S segments in the Cu_2S NWs after Ag^+ exchange for 6, 24, 48, and 60 s. Cu_2S and Ag_2S show substantial contrast difference in the TEM images, which facilitates the direct monitoring of the rate of Ag_2S segment growth. By STEM-EDS mapping, the brighter region is confirmed to be composed of Ag_2S and the darker regions around it as Cu_2S (Figure 3f). Remarkably, large and uniform Ag_2S blocks about 100 nm in length were observed after 24 s of reaction. This indicates that the Ag_2S segments grow rapidly; many of the Ag_2S segments merge to form long but clearly separated Ag_2S blocks. A precise control of the time of the cation exchange process is critical in producing such superlattice NWs. After 48 s of reaction, the Ag_2S segments lengthened further and became the dominant component of the wires

and only narrow strips of Cu_2S remained. Complete conversion of the NWs into Ag_2S NWs was achieved after 60 s of reaction. XRD patterns were taken to verify the composition of the Cu_2S–Ag_2S superlattice NWs and the final Ag_2S NWs (see Supporting Information Figure S3). From Figure 3b, it is apparent that the newly formed Ag_2S segments are largely parallel to the twin boundary planes, which are perpendicular to the growth direction of Cu_2S nanowires. From an energetic point of view, twin boundaries are likely to be the preferred sites for cation exchange. Supporting Information Figure S6 illustrates the cation exchange process to generate Ag_2S segments on a Cu_2S NW. Ag ions diffuse through the $(1\bar{1}1)$ twin boundary sites into a NW and form thin Ag_2S strips initially. Continuous Ag ion migration outward from the thin strips and Cu ion dissolution into the solution leads to the elongation of the Ag_2S segments.

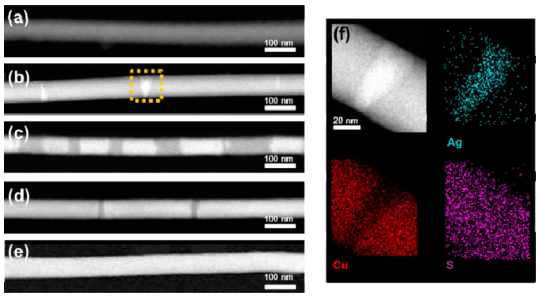

Figure 3. Cu_2S–Ag_2S superlattice NWs with different Ag_2S segment lengths. (a–e) STEM high-angle annular dark-field (HAADF) images of the Cu_2S–Ag_2S superlattice NWs formed after Cu_2S NWs react with the Ag cation at room temperature. The times used for the cation exchange process are (a) 0 s, (b) 6 s, (c) 24 s, (d) 48 s, (e) 60 s. (f) STEM-EDS mapping for the framed region shown in panel b. Ag signals are confined to the bright stripe regions. Cu signals are located in the darker regions. Sulfur is uniformly distributed throughout the entire NW.

The structures of Ag_2S–Cu_2S heterojunctions were examined by TEM and diffraction analysis of FFT patterns (Figures 4a and S7). The red dashed line in Figure 4a indicates the border between Ag_2S (left) and Cu_2S (right) segments with clearly different lattice structures for the two regions. FFT patterns taken from both regions show that the Ag_2S $(00\bar{2})$ lattice planes are parallel to the $(1\bar{1}1)$ planes of Cu_2S. Additional examination of the transitional region by FFT processing of the HRTEM image reveals the presence of dislocations in both the Cu_2S and Ag_2S segments (see Supporting Information Figures S8–S11). The Cu_2S segment contains dislocations along the [220] direction, while the Ag_2S segment has dislocations along the [002] direction. The large and rapid lattice change from a fcc structure to a monoclinic structure leads to these imperfections throughout the Ag_2S

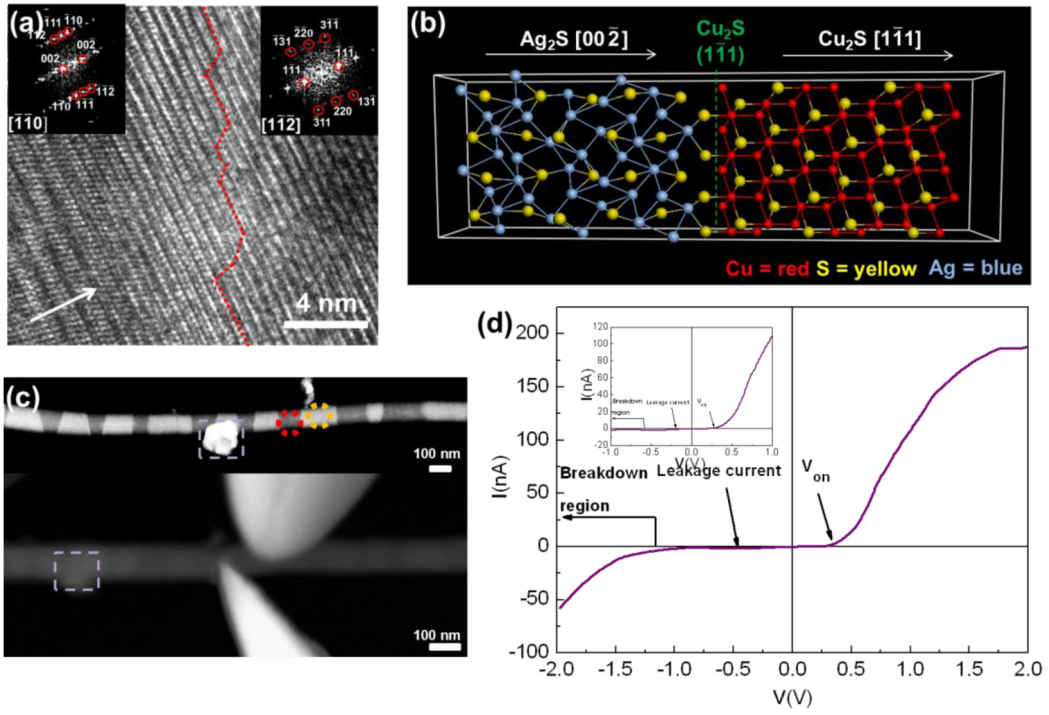

Figure 4. Crystal structure model of the Ag_2S–Cu_2S heterojunction and electrical measurement of the NW. (a) HRTEM image and FFT patterns of a Ag_2S–Cu_2S heterojunction. Zone axes for these FFT patterns are given. The left portion of the red dashed line is the Ag_2S region, while the right portion is the Cu_2S region. The arrow indicates the NW growth direction. (b) Crystal structure model of a Ag_2S–Cu_2S p–n heterojunction. The crystal lattice directions are indicated. (c) STEM (top) and SEM (bottom) images of a single superlattice NW before and during the contact of tungsten probes. The red circle (or darker region) refers to the Cu_2S segment, while the yellow circle (brighter region) indicates the Ag_2S region. The light purple frame indicates dirt near the NW as a marker to ensure that the right p–n position is probed. (d) *I*–*V* curve of the p–n heterojunction.

segments and the Cu_2S regions near the heterojunctions. The presence of a high density of dislocations also accounts for the low peak intensities in the XRD patterns of the NWs. Figure 4b presents an atomic model of the Ag_2S-Cu_2S heterojunction, showing that the $(00\bar{2})$ lattice planes of Ag_2S are aligned to the $(1\bar{1}1)$ planes of Cu_2S.

To confirm that the present two-step process forms the Cu_2S-Ag_2S superlattice structure, monoclinic structure Cu_2S NWs were grown by a hydrothermal process.[28] Twins were also observed in the monoclinic Cu_2S NWs. In contrast to that of fcc NWs, twin planes are not perpendicular to the growth direction, as seen in Supporting Information Figure S12. The observation of irregular segments of Ag_2S in monoclinic Cu_2S, through cation exchange, is consistent with the suggestion that twin boundaries are preferred sites for cation exchange. Examples are shown in Supporting Information Figures S13 and S14. The finding further shows the present two-step ion exchange process forming first fcc Cu_2S NWs as desirable templates for successful generation of a regular Cu_2S-Ag_2S superlattice structure.

The presence of alternating Cu_2S segments and Ag_2S segments results in the formation of NWs with many p−n heterojunctions. To verify the formation of p−n heterojuctions, *I*−*V* measurements were carried out on adjacent Cu_2S and Ag_2S blocks in a superlattice structure. Figure 4c shows that two tungsten tips are in contact with the darker Cu_2S and brighter Ag_2S regions. The brightness difference is due to *Z*-contrast in scanning electron microscope (SEM) imaging. Such tungsten probes, although having quite large tips, have been used to measure electrical conductivity of a single Cu_2O nanocube and octahedron.[29] The recorded *I*−*V* curve, as shown in Figure 4d, is typical for a p−n junction with a turn-on voltage of 0.6 V under forward bias. Under reverse bias, the p−n heterojunction has a very low leakage current, and breakdown occurs at around −1.25 V. The results show that multiple p−n junctions within a NW can be directly fabricated by sequential cation exchange processes, and the p- and n-type segment lengths can be controlled by terminating cation exchange at precise times.

CONCLUSIONS

In summary, we have demonstrated that twins created in the cation exchange process of NWs can be utilized to generate heterostructures in the chain cation exchange steps. By properly choosing the compositions of the heterojunctions constituting the NWs, such as the formation of $(1\bar{1}1)$ twins in Cu_2S NWs from CdS NWs, and conversion of the Cu_2S NWs to Cu_2S-Ag_2S NWs, superlattice NWs with multiple p−n junctions can be fabricated. The precise control of the extent of n-type and p-type segments of the NWs by a solution method at room temperature with varying reaction time has the potential to be generalized as a facile method to form various functional heterojunctions.

EXPERIMENTAL METHODS

CdS NW Synthesis. CdS NWs were grown along the [110] direction with a VLS process. CdS powder (99.999%, Alfa Aesar) and the Au-coated (10 nm) Si substrate were placed, respectively, at the 800 and 650 °C zone with Ar flow (100 sccm).

Chain Phase Transformation. CdS NWs were dipped into ethylene glycol (99.5%, Sigma-Aldrich) containing 0.5 M CuCl (99%, Alfa Aesar) at 75 °C. After 25 min, the CdS NWs completely transformed to Cu_2S NWs with a high density of twins. The Cu_2S NWs were then dipped into ethylene glycol containing 0.05 M $AgNO_3$ (99.8%, Showa) at room temperature and formed Ag_2S segments in Cu_2S NWs within 1 min.

Instrumentation. XRD patterns were recorded using a Bruker D2 phaser X-ray diffractometer. FE-SEM images were obtained with the use of a FEI Helios 1200^+. TEM images were obtained using JEOL ARM200F and 2010F electron microscopes.[30]

Electrical Measurements. Tungsten wires (99.95%, Alfa Aesar) were used to make 100 nm tungsten tips by electrodecomposition in a 2 M KOH (Sigma-Aldrich) solution under DC power. *I*−*V* measurements were performed with a Keithley model 4200-SCS source measurement unit. Tungsten tips were installed on a nanomanipulator (Kammrath & Wiess GmbH). The nanomanipulator was loaded inside a JEOL 7000F scanning electron microscope.

Conflict of Interest: The authors declare no competing financial interest.

Acknowledgment. We thank K.L. Lin and C.C. Chen at the National Nano Device Laboratories for discussion of experimental results, and W.N. Lee at the Center for Nanotechnology, Material Science and Microsystems, NTHU, for help in nanoprobe *I*−*V* measurements. The authors are grateful for the research support from the Ministry of Science and Technology of Taiwan under project number MOST 102-2221-E-007-145 and MOST 102-2633-M-007-002.

Supporting Information Available: Additional figures. This material is available free of charge *via* the Internet at http://pubs.acs.org.

REFERENCES AND NOTES

1. Wu, Y.; Xiang, J.; Yang, C.; Lu, W.; Lieber, C. M. Single-Crystal Metallic Nanowires and Metal/Semiconductor Nanowire Heterostructures. *Nature* **2004**, *430*, 61–65.
2. Chen, C.; Cai, W.; Long, M.; Zhou, B.; Wu, Y.; Wu, D.; Feng, Y. Synthesis of Visible-Light Responsive Graphene Oxide/TiO_2 Composites with p/n Heterojunction. *ACS Nano* **2010**, *4*, 6425–6432.
3. Wu, J. L.; Chen, F. C.; Hsiao, Y. S.; Chien, F. C.; Chen, P.; Kuo, C. H.; Huang, M. H.; Hsu, C. S. Surface Plasmonic Effects of Metallic Nanoparticles on the Performance of Polymer Bulk Heterojunction Solar Cells. *ACS Nano* **2011**, *5*, 959–967.
4. Dennler, G.; Scharber, M. C.; Brabec, C. J. Polymer-Fullerene Bulk-Heterojunction Solar Cells. *Adv. Mater.* **2009**, *21*, 1323–1338.
5. Zhang, W.; Jin, W.; Fukushima, T.; Saeki, A.; Seki, S.; Aida, T. Supramolecular Linear Heterojunction Composed of Graphite-like Semiconducting Nanotubular Segments. *Science* **2011**, *334*, 340–343.

6. Gao, P. X.; Ding, Y.; Mai, W.; Hughes, W. L.; Lao, C.; Wang, Z. L. Conversion of Zinc Oxide Nanobelts into Superlattice-Structured Nanohelices. *Science* **2005**, *309*, 1700–1704.
7. Papagno, M.; Rusponi, S.; Sheverdyaeva, P. M.; Vlaic, S.; Etzkorn, M.; Pacilé, D.; Moras, P.; Carbone, C.; Brune, H. Large Band Gap Opening between Graphene Dirac Cones Induced by Na Adsorption onto an Ir Superlattice. *ACS Nano* **2012**, *6*, 199–204.
8. Caroff, P.; Dick, K. A.; Johansson, J.; Messing, M. E.; Deppert, K.; Samuelson, L. Controlled Polytypic and Twin-Plane Superlattices in III–V Nanowires. *Nat. Nanotechnol.* **2008**, *4*, 50–55.
9. Zhang, Q.; Xie, J.; Yang, J.; Lee, J. Y. Monodisperse Icosahedral Ag, Au, and Pd Nanoparticles: Size Control Strategy and Superlattice Formation. *ACS Nano* **2008**, *3*, 139–148.
10. Chen, Z.; O'Brien, S. Structure Direction of II–VI Semiconductor Quantum Dot Binary Nanoparticle Superlattices by Tuning Radius Ratio. *ACS Nano* **2008**, *2*, 1219–1229.
11. Xiang, J.; Lu, W.; Hu, Y.; Wu, Y.; Yan, H.; Lieber, C. M. Ge/Si Nanowire Heterostructures as High-Performance Field-Effect Transistors. *Nature* **2006**, *441*, 489–493.
12. Tian, B.; Zheng, X.; Kempa, T. J.; Fang, Y.; Yu, N.; Yu, G.; Huang, J.; Lieber, C. M. Coaxial Silicon Nanowires as Solar Cells and Nanoelectronic Power Sources. *Nature* **2007**, *449*, 885–889.
13. Tang, J.; Huo, Z.; Brittman, S.; Gao, H.; Yang, P. Solution-Processed Core–Shell Nanowires for Efficient Photovoltaic Cells. *Nat. Nanotechnol.* **2011**, *6*, 568–572.
14. Li, Y.; Qian, F.; Xiang, J.; Lieber, C. M. Nanowire Electronic and Optoelectronic Devices. *Mater. Today* **2006**, *9*, 18–27.
15. Yan, R.; Gargas, D.; Yang, P. Nanowire Photonics. *Nat. Photonics* **2009**, *3*, 569–576.
16. Carbone, L.; Cozzoli, P. D. Colloidal Heterostructured Nanocrystals: Synthesis and Growth Mechanisms. *Nano Today* **2010**, *5*, 449–493.
17. Gudiksen, M. S.; Lauhon, L. J.; Wang, J.; Smith, D. C.; Lieber, C. M. Growth of Nanowire Superlattice Structures for Nanoscale Photonics and Electronics. *Nature* **2002**, *415*, 617–620.
18. Wu, Y.; Fan, R.; Yang, P. Block-by-Block Growth of Single-Crystalline Si/SiGe Superlattice Nanowires. *Nano Lett.* **2002**, *2*, 83–86.
19. Tian, B.; Xie, P.; Kempa, T. J.; Bell, D. C.; Lieber, C. M. Single-Crystalline Kinked Semiconductor Nanowire Superstructures. *Nat. Nanotechnol.* **2009**, *4*, 824–829.
20. Robinson, R. D.; Sadtler, B.; Demchenko, D. O.; Erdonmez, C. K.; Wang, L. W.; Alivisatos, A. P. Spontaneous Superlattice Formation in Nanorods through Partial Cation Exchange. *Science* **2007**, *317*, 355–358.
21. Sadtler, B.; Demchenko, D. O.; Zheng, H.; Hughes, S. M.; Merkle, M. G.; Dahmen, U.; Wang, L. W.; Alivisatos, A. P. Selective Facet Reactivity during Cation Exchange in Cadmium Sulfide Nanorods. *J. Am. Chem. Soc.* **2009**, *131*, 5285–5293.
22. Demchenko, D. O.; Robinson, R. D.; Sadtler, B.; Erdonmez, C. K.; Alivisatos, A. P.; Wang, L. W. Formation Mechanism and Properties of CdS–Ag_2S Nanorod Superlattices. *ACS Nano* **2008**, *2*, 627–636.
23. Luther, J. M.; Zheng, H.; Sadtler, B.; Alivisatos, A. P. Synthesis of PbS Nanorods and Other Ionic Nanocrystals of Complex Morphology by Sequential Cation Exchange Reactions. *J. Am. Chem. Soc.* **2009**, *131*, 16851–16857.
24. Son, D. H.; Hughes, S. M.; Yin, Y.; Alivisatos, A. P. Cation Exchange Reactions in Ionic Nanocrystals. *Science* **2004**, *306*, 1009–1012.
25. Ertekin, E.; Greaney, P. A.; Chrzan, D. C.; Sands, T. D. Equilibrium Limits of Coherency in Strained Nanowire Heterostructures. *J. Appl. Phys.* **2005**, *97*, 114325.
26. Chen, K. C.; Wu, W. W.; Liao, C. N.; Chen, L. J.; Tu, K. N. Observation of Atomic Diffusion at Twin-Modified Grain Boundaries in Copper. *Science* **2008**, *321*, 1066–1069.
27. Wagner, R. S.; Ellis, W. C. Vapor–Liquid–Solid Mechanism of Single Crystal Growth. *Appl. Phys. Lett.* **1964**, *4*, 89–90.
28. Lai, C. H.; Lu, M. Y.; Chen, L. J. Metal Sulfide Nanostructures: Synthesis, Properties and Applications in Energy Conversion And Storage. *J. Mater. Chem.* **2012**, *22*, 19–30.
29. Kuo, C. H.; Yang, Y. C.; Gwo, S.; Huang, M. H. Facet-Dependent and Au Nanocrystal-Enhanced Electrical and Photocatalytic Properties of Au–Cu_2O Core–Shell Heterostructures. *J. Am. Chem. Soc.* **2011**, *133*, 1052–1057.
30. Lu, Y. J.; Kim, J.; Chen, H. Y.; Wu, C.; Dabidian, N.; Sanders, C. E.; Wang, C. Y.; Lu, M. Y.; Li, B. H.; Qiu, X.; *et al.* Plasmonic Nanolaser Using Epitaxially Grown Silver Film. *Science* **2012**, *337*, 450–453.